Spectral characteristics of the response of the meridional overturning circulation to deep water formation

Julie Deshayes, Claude Frankignoul

Spectral Characteristics of the Response of the Meridional Overturning Circulation to Deep-Water Formation

JULIE DESHAYES AND CLAUDE FRANKIGNOUL

LOCEAN Unité Mixte de Recherche, CNRS–IRD–UPMC, Université Pierre et Marie Curie, Paris, France

(Manuscript received 26 October 2004, in final form 25 March 2005)

ABSTRACT

The response of the upper limb of the meridional overturning circulation to the variability of deep-water formation is investigated analytically with a linear, reduced-gravity model in basins of simple geometry. The spectral characteristics of the model response are first derived by prescribing white-noise fluctuations in the meridional transport at the northern boundary. Although low-frequency basin modes are solutions to the eigenproblem, they are too dissipative to be significantly excited by the boundary forcing, and the thermocline depth response has a red spectrum with no prevailing time scale other than that of a high-frequency equatorial mode, only flattening at the millennial time scale because of vertical diffusivity. The meridional transport is asymmetric about the equator because the northern part of the basin is directly influenced by the boundary forcing while the southern part is mostly set in motion by long Rossby waves. This results in the equator acting as a low-pass filter for the Southern Hemisphere, which clarifies the so-called buffering effect of the equator. In a basin connected by a southern circumpolar channel, the thermocline depth and the transport spectra are redder than in the forced basin and, when a somewhat more realistic stochastic forcing derived from general circulation model simulations is considered, the variability is strongly reduced at high frequency. The linear model qualitatively explains several features of the low-frequency variability of the meridional overturning circulation in climate models, such as its red spectrum and its larger intensity in the North Atlantic Ocean.

1. Introduction

The meridional overturning circulation (MOC) is an important element of the global climate system because it transports a substantial amount of heat from low latitudes to high latitudes [about 1.3×10^{15} W in the Atlantic Ocean at 25°N according to Ganachaud and Wunsch (2000)]. Although it is not clear to what extent changes of the MOC were responsible for the strong fluctuations of the last glacial period (Boyle 2000), variations of the intensity of the MOC are likely to change the climate significantly (e.g., Manabe and Stouffer 1999). However, its main time scales and mechanisms of variability are poorly known. The observations are too sparse to document the MOC time scales, but simulations with realistic climate models provide useful guidance, albeit with some model dependence. Delworth et al. (1993) found that the natural variability of the MOC in the Geophysical Fluid Dynamics Laboratory climate model had an enhanced variance in a fairly broad frequency band around 50-yr period that seemed to be linked to the advection of salinity anomalies by the wind-driven circulation in the sinking regions, but a longer simulation showed that the maximum variance was at periods of 70–100 yr and that the MOC variability primarily reflected the oceanic response to the low-frequency surface heat flux forcing (Delworth and Greatbatch 2000). Timmermann and Latif (1998) suggested that an active ocean–atmosphere coupling at high northern latitudes explained the dominant 35-yr period of the MOC variability in another coarse-resolution climate model. On the other hand, Bentsen et al. (2004) found no clear evidence of an active coupling with the atmosphere in the higher-resolution Bergen Climate Model. They suggested that the MOC variability was forced by the atmosphere through deep convection at high latitudes and was characterized by a red spectrum with a substantial amount of variance at periods from 10 to 100 yr, without any

Corresponding author address: Dr. Julie Deshayes, LOCEAN (LODYC), UPMC, Boite 100, 4 place Jussieu, 75252 Paris, France.
E-mail: julie.deshayes@lodyc.jussieu.fr

significant spectral peak. The advection of salinity anomalies from the Tropics to the northern North Atlantic has also been suggested as a cause of low-frequency MOC variability (Latif et al. 2000; Vellinga and Wu 2004; Mignot and Frankignoul 2005).

In most of these modeling studies, the changes in the deep-water production are assumed to be the main cause of MOC variability. However, the MOC and the rate of deep-water formation may not be tightly linked on the decadal time scale (Mauritzen and Häkkinen 1999). Observations also suggest that the deep transport variability may not be directly related to deep-water production (Schott et al. 2004). In addition, as the variability of the Ekman transport drives the MOC on short time scales, wind forcing in the North Atlantic (e.g., Eden and Willebrand 2001) and in the Southern Ocean (e.g., Rahmstorf 1997) also plays a role. In view of this complexity, some understanding of the MOC dynamics may be gained by separating the purely oceanic processes that affect the MOC response to changes in deep-water formation from those that control deep-water formation itself and are more affected by nonlinearities, air–sea interactions, and feedback processes. In the present paper, we thus consider deep-water formation as a prescribed external forcing and focus on the oceanic response to this forcing.

Simplified theoretical models have long been used to explore the essential role played by oceanic waves in the ocean response to changes in deep-water formation. Using a 1½-layer model with a moving deep layer to study the adjustment to a sudden change in deep-water formation, Kawase (1987) showed that Kelvin waves first propagated southward along the western boundary to the equator, then eastward along the equator, and poleward at the eastern boundary. The poleward propagation of the Kelvin waves generates westward-propagating long Rossby waves that drive the interior flow. In the limit of very weak damping, the flow spins up to the steady state of Stommel and Arons (1960). Huang et al. (2000) used a similar model (but with a moving upper layer in several basins) to study the global adjustment of the thermocline to a sudden change in deep-water formation. The signal was again propagated by fast Kelvin waves, which also connected the Atlantic basin to the others by eastward propagation along the southern tip of the continents, and by slow Rossby waves that radiated in the interior of the basins. The latter resulted in a centennial time scale for the adjustment of the World Ocean, which is shorter than what is expected from a global adjustment set by advection processes.

The 1½-layer model was also used by Johnson and Marshall (2002a, hereinafter JM02) to study the adjustment of the Atlantic to a change in the volume transport across the northern boundary, reflecting a change in deep-water formation. JM02 showed that the buffering effect of the equator leads to a north–south asymmetry in the meridional transport. As the equator acts as a barrier to the southward propagation of Kelvin waves along the western boundary, the meridional transport in the Southern Hemisphere is exclusively set up by Rossby waves emanating from the eastern boundary. Because of the restriction on zonal pressure gradients imposed by the equatorial region, only a small portion of the meridional transport perturbation is communicated to the South Atlantic at any one time. The implication is that the South Atlantic, as the rest of the global ocean, adjusts on much longer time scales than the North Atlantic, which rapidly responds to changes in deep-water formation.

If the low-frequency variability of the MOC is primarily determined by the long Rossby waves, one would expect to observe the decadal baroclinic basin modes first discussed by Lacasce (2000) and Cessi and Primeau (2001). In a closed basin, the eigenfrequencies are a multiple of the frequency of the gravest mode, which has a period close to the basin transit time of the long Rossby waves. These low-frequency modes are strongly damped in basins in which the transit time is latitude dependent (Primeau 2002), but their amplitude can be substantial when forced by a wind stress of optimal pattern (Cessi and Louazel 2001, hereinafter CL01; Cessi and Otheguy 2003). Here, we show that these modes are not significantly excited by changes in deep-water formation.

In this paper, we focus on the spectral characteristics of the MOC in response to the variability of deep-water formation. This study extends the work of JM02, who considered the adjustment problem. It parallels and is consistent with Johnson and Marshall (2002b, 2004), who considered the case of a periodic forcing. However, we consider the oceanic response to a continuum of forcing frequencies and clarify the frequency dependence of the equatorial buffer and the role of the western boundary currents. In addition, we take into account the influence of vertical diffusivity on the variability of the MOC.

We use a linear 1½-layer model of the upper thermocline water variability, which is close to the simplest models considered by JM02 and CL01, who showed that linearization provides an acceptable approximation to the full dynamics. Changes in deep-water formation take place north of the basin and are represented by the compensating meridional transport in the upper layer, prescribed at the northern boundary. The model, described in section 2, is driven by stochastic

changes in the meridional transport. In section 3, the spectral characteristics of the model response to white-noise forcing are investigated in the one-interhemispheric-basin case. In section 4, we investigate the variability in two basins connected by a southern circumpolar channel. In section 5, we use a more realistic forcing spectrum. Conclusions are given in section 6.

2. The model

The basin is rectangular, is 4000 km wide, and extends from 45°S to 65°N. The boundary condition at the eastern, southern, and western boundaries is no normal flow. At the northern boundary, the zonally integrated meridional transport $T_N(t)$ is prescribed and represents changes in the production of deep water. It is implicitly assumed to be concentrated near the western boundary, or equivalently that perturbations in volume transport are propagated infinitely fast along the northern boundary.

The equations are the linear reduced-gravity shallow-water equations. As the inclusion of wind forcing would not alter the essential dynamics of the Rossby waves (according to JM02), we neglect the latter and consider a basic state at rest. The flow is initiated by the propagation of baroclinic Kelvin waves from the deep-water production region along the western boundary, then along the equator, and finally along the eastern boundary. Since this first phase only takes few months (Kawase 1987), we assume for simplicity, as in JM02, that the Kelvin waves are infinitely fast and only consider the slower propagation of the long Rossby waves across the basin, which takes a decade at midlatitudes. Then, we can simplify the problem considerably and assume the geostrophic balance in the interior:

$$f\upsilon = g' \frac{\partial h}{\partial x}; fu = -g' \frac{\partial h}{\partial y}, \tag{1}$$

where u, υ, and h denote the perturbations in zonal velocity, meridional velocity, and interface depth around the mean state, $g' = 0.02$ m s^{-2} is the reduced gravity, and $f = \beta y$ is the Coriolis parameter ($\beta = 2.28 \times 10^{-11}$ s^{-1}).

Vertical diffusivity is represented by a Newtonian damping in the linear continuity equation

$$\frac{\partial h}{\partial t} + H\frac{\partial u}{\partial x} + H\frac{\partial \upsilon}{\partial y} = -\lambda h, \tag{2}$$

where $H = 500$ m is the mean interface depth and $\lambda = 4 \times 10^{-10}$ s^{-1} is the coefficient of vertical diffusivity. The latter value was used by Huang et al. (2000) and corresponds to a vertical mixing of $\lambda \times H^2 = 1$ cm^2 s^{-1}, setting our model in Kawase's (1987) limit of very weak damping. Introducing (1) in (2) gives

$$\frac{\partial h}{\partial t} - c\frac{\partial h}{\partial x} = -\lambda h, \tag{3}$$

where

$$c(y) = \frac{\beta g' H}{f^2(y)}$$

is the speed of the long Rossby waves. This expression is not valid at the equator, but equatorial dynamics indicate that the speed of the Rossby waves is bounded by one-third of the speed of the Kelvin waves. Thus we limit the Rossby wave velocity by $\sqrt{g'H}/3$ and avoid singularities near the equator.

Solving (3) gives $h(x, y, t)$ in the interior as

$$h(x, y, t) = h_e\left[t - \frac{L_x - x}{c(y)}\right] \exp\left\{-\lambda\left[\frac{L_x - x}{c(y)}\right]\right\}, \tag{4}$$

where $x = 0$ at the western boundary and h_e is the interface depth perturbation at the eastern boundary $x = L_x$, which only depends on t since the zonal flow must vanish. In the interior, $h(x, y, t)$ is determined by the westward propagation of the eastern boundary perturbations by the long Rossby waves, attenuated by vertical diffusivity. Near the western boundary, that is, for $0 < x < x_b$, where x_b is the eastern limit of the western boundary layer, dissipation is required in (1) in order to close the circulation. Note that the interior solution is not valid close to the southern boundary because of the no-normal-flow condition. However, as the thickness of the southern boundary layer is very small relative to the length of the basin (CL01), the condition of no normal flow is equivalent to prescribing a null integrated meridional transport, as done here.

The zonal integration of the mass conservation (2) gives

$$\int_0^{L_x}\left[\frac{\partial h}{\partial t}(x, y, t) + \lambda h(x, y, t)\right] dx = -\frac{\partial}{\partial y} T(y, t), \tag{5}$$

where $T(y, t)$ is the meridional volume transport. As in JM02, we assume that the volume of the western boundary layer is negligible with regard to the interior volume, and, using (3), we obtain

$$c(y)\left\{h_e(t) - h_e\left[t - \frac{L_x}{c(y)}\right] \exp\left[-\lambda\frac{L_x}{c(y)}\right]\right\} = -\frac{\partial}{\partial y} T(y, t). \tag{6}$$

Integrating from the southern edge y_s (45°S) to the northern edge y_n (65°N) of the basin leads to

$$h_e(t) = \frac{1}{\int_{y_s}^{y_n} c(y)\,dy}\left\{\int_{y_s}^{y_n} c(y) h_e\left[t - \frac{L_x}{c(y)}\right] \times \exp\left[-\lambda \frac{L_x}{c(y)}\right] dy - T_N(t)\right\} \quad (7)$$

since $T(y_s, t) = 0$ and $T(y_n, t) = T_N(t)$. Equation (7) is the same as obtained by JM02, if $\lambda = 0$, and is a delay equation for the depth anomaly at the eastern boundary, from which the anomaly in the entire basin can be calculated. It reflects that, in the model, perturbations in the volume transport at the northern boundary are propagated infinitely fast to the eastern boundary and then slowly westward by the Rossby waves (and dissipated by vertical diffusivity). When the Rossby waves reach the western boundary, the perturbations are instantly transmitted back to the eastern boundary, and again radiated westward.

The meridional transport is given by integration of (6) from the northern or southern boundary, yielding the two expressions

$$T(y, t) = T_N(t) + \int_{y}^{y_n} c(y)\left\{h_e(t) - h_e\left[t - \frac{L_x}{c(y)}\right] \times \exp\left[-\lambda \frac{L_x}{c(y)}\right]\right\} dy \quad \text{and} \quad (8)$$

$$T(y, t) = -\int_{y_s}^{y} c(y)\left\{h_e(t) - h_e\left[t - \frac{L_x}{c(y)}\right] \times \exp\left[-\lambda \frac{L_x}{c(y)}\right]\right\} dy. \quad (9)$$

As the meridional velocity remains geostrophic to a good approximation in the western boundary layer, we will also use the geostrophic approximation for T away from the equator, which becomes after linearization

$$T(y, t) \approx \frac{g' H}{f(y)}[h_e(t) - h(0, y, t)], \quad (10)$$

where $h(0, y, t)$ could be obtained by resolving the dynamics of the western boundary layer.

The meridional transport is the sum of the interior transport T_I and the transport in the western boundary layer T_{BL}. As the interior perturbations in the two hemispheres are synchronously forced by the eastern boundary, T_I is symmetric about the equator. On the other hand, T is not symmetric about the equator because of the southern and northern boundary conditions. The asymmetry is due to T_{BL}, but the latter does not need to be calculated for our purpose.

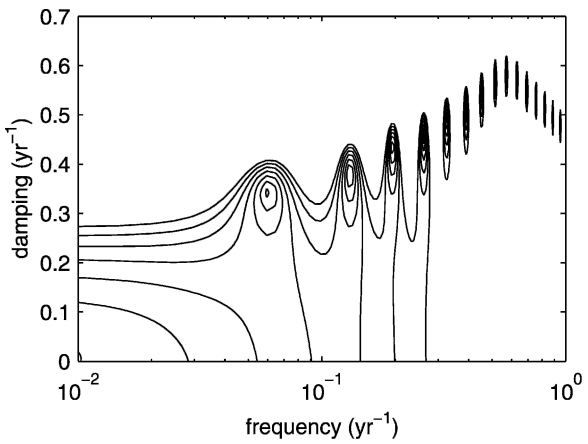

FIG. 1. Modulus of the lhs of (14) vs the real part of the frequency [Re(ω)/2π] and the damping time [Im(ω)], with the bull's-eyes indicating the minima.

The eigenmodes are unforced solutions to the model when imposing global mass conservation:

$$\int_{y_s}^{y_n}\int_{0}^{L_x} h(x, y, t)\,dx\,dy = 0. \quad (11)$$

As shown in CL01, the interior solution (4) can be used to a good approximation in (11) in the limit of weak friction, yielding

$$\int_{y_s}^{y_n}\int_{0}^{L_x} h_e\left[t - \frac{L_x - x}{c(y)}\right] \exp\left\{-\lambda\left[\frac{L_x - x}{c(y)}\right]\right\} dx\,dy = 0. \quad (12)$$

To determine the eigenvalues, we look for solutions of the form $h_e(t) = \mathrm{Re}[\hat{h}e(\omega)e^{i\omega t}]$, where Re indicates real part. Introduction in (4) gives the interior eigenfunction

$$\hat{h}(x, y, \omega) = \hat{h}_e(\omega) \exp\left[-(\lambda + i\omega)\frac{L_x - x}{c(y)}\right], \quad (13)$$

where the longitudinal wavelength $2\pi c(y)/\mathrm{Re}(\omega)$ decreases with latitude. Solving the x integral in (12) yields the eigenvalues equation

$$\int_{y_s}^{y_n} c(y)\left\{1 - \exp\left[-(\lambda + i\omega)\frac{L_x}{c(y)}\right]\right\} dy = 0. \quad (14)$$

As discussed in CL01, if ω were real, the real part of the integral in (14) would be strictly positive and there would be no solution. The frequency ω is thus complex, and the eigenmodes are damped. The low-frequency solutions are shown by the minima in Fig. 1, where the period of the gravest eigenmode is 16.7 yr, which is close to the Rossby waves transit time across the basin at the northern boundary (15 yr). The modes are strongly dissipated; the exponential decay time for the

gravest eigenmode is 2.9 yr, because of the strong latitude dependence of the Rossby waves' transit time across the basin (Primeau 2002). The interior eigenfunction is symmetric about the equator and has a large spatial scale: the lowest-frequency eigenmode has a zonal wavelength that goes from 4000 km at the northern edge to 50 000 km at the equator. The meridional wavelength is equal to the basin length at the eastern boundary and decreases westward at a rate that increases with the eigenvalue.

In addition, (14) also has a nearly real solution because c was assumed to be constant in the vicinity of the equator. The period of this mode corresponds to the transit time of the equatorial Rossby waves (44 days) and the damping is very small. Its zonal scale varies from 200 km at the northern edge to 3000 km at the equator.

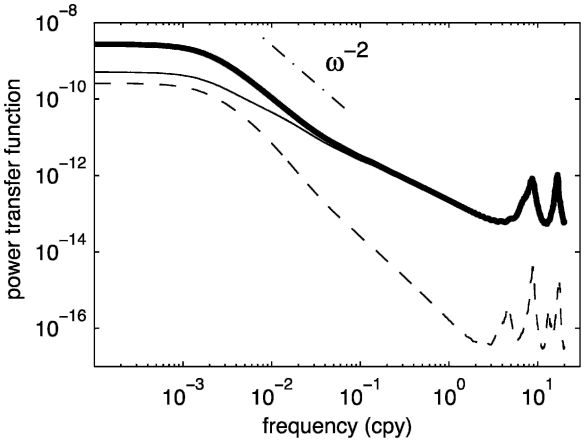

FIG. 2. Power transfer function for h_e (no unit) in the one-basin case (thick line), and in basin A (thin plain line) and P (thin dashed line) of the two-basin case. The mixed line indicates an ω^{-2} law.

3. Variability in one basin

The model is forced by stochastic fluctuations in T_N, which reflect changes in deep-water formation. To focus on the dynamics, we first consider the transfer function of the model, which is equivalent to investigating its response to white-noise forcing. As the model is linear, it is straightforward to investigate its response to a more realistic forcing (section 5).

Denoting Fourier transform by a caret, one has $[T_N(t), h_e(t)] = [1/(2\pi)] \int_{-\infty}^{+\infty} [\widehat{T_N}(\omega), \hat{h}_e(\omega)] e^{i\omega t}\, d\omega$. Replacing in (7) yields

$$\hat{h}_e(\omega) = \frac{-\widehat{T_N}(\omega)}{\displaystyle\int_{y_s}^{y_n} c(y)\left\{1 - \exp\left[-(\lambda + i\omega)\frac{L_x}{c(y)}\right]\right\} dy}. \tag{15}$$

Since the frequency spectrum of a function F is defined by $S_F(\omega)\delta(\omega - \omega') = \langle \hat{F}(\omega)\hat{F}^*(\omega')\rangle$, where the asterisk denotes complex conjugate and the angle brackets denote the expectation operator, the spectrum of h_e is given by that of the forcing times the power transfer function

$$D_{h_e}(\omega) = \left(\int_{y_s}^{y_n} c(y)\left\{1 - \exp\left[-(\lambda + i\omega)\frac{L_x}{c(y)}\right]\right\} dy \times \int_{y_s}^{y_n} c(y)\left\{1 - \exp\left[-(\lambda - i\omega)\frac{L_x}{c(y)}\right]\right\} dy\right)^{-1}, \tag{16}$$

which is represented in Fig. 2 (thick line). Note that what we call power transfer function is the square modulus of the transfer function for linear time-invariant filters as defined by Percival and Walden (1993).

The model resonates if

$$\int_{y_s}^{y_n} c(y)\left\{1 - \exp\left[-(\lambda + i\omega)\frac{L_x}{c(y)}\right]\right\} dy = 0,$$

which is the eigenvalue equation of (14). As we have seen, the equatorial mode is an approximate solution for real ω, corresponding to the high-frequency peaks in Fig. 2 (as the mode is not sinusoidal, the higher harmonic also appears in the spectrum). At periods from about 4 months to 20 yr, D_{h_e} approximately varies as ω^{-1}. At periods longer than the basin transit time of the slowest Rossby waves, one has $\omega \ll c(y)/L_x$ and

$$D_{h_e} \approx \frac{1}{L_x L_y}\frac{1}{\lambda^2 + \omega^2}.$$

This corresponds to a first-order Markov process; D_{h_e} varies as ω^{-2} as the model behaves as an integrator, and it flattens at periods $\gtrsim$1000 yr when the forcing is balanced by vertical diffusivity.

For the chosen geometry, the low-frequency basin modes are too dissipative to be significantly excited by changes in deep-water formation. This also holds for the sector ocean of Johnson and Marshall (2004) because their range of Rossby wave basin transit time is the same as that for a rectangular basin in the equatorial β-plane approximation (Cessi and Otheguy 2003), and it applies to the Atlantic. If the basin was much narrower at high latitudes, the transit time would vary less with latitude and the gravest mode would resonate. Thus the basin modes should be more easily excited in the North Pacific where the longitudinal range is much

shorter at high latitudes than at low latitudes (Primeau 2002).

The interior solution (13) is symmetric about the equator, but the solution in the western boundary layer is not, so that the spectrum of the meridional transport depends on latitude. From (8) or (9), the power spectrum of the meridional transport is related to that of the forcing via the power transfer function D_T, given by

$$D_T(y,\omega)=\frac{\displaystyle\int_{y_s}^{y} c(y)\left\{1-\exp\left[-(\lambda+i\omega)\frac{L_x}{c(y)}\right]\right\}dy\times\int_{y_s}^{y} c(y)\left\{1-\exp\left[-(\lambda-i\omega)\frac{L_x}{c(y)}\right]\right\}dy}{\displaystyle\int_{y_s}^{y_n} c(y)\left\{1-\exp\left[-(\lambda+i\omega)\frac{L_x}{c(y)}\right]\right\}dy\times\int_{y_s}^{y_n} c(y)\left\{1-\exp\left[-(\lambda-i\omega)\frac{L_x}{c(y)}\right]\right\}dy}, \tag{17}$$

which is represented in Fig. 3 (bottom) at several latitudes. Overall, D_T is much larger in the Northern Hemisphere than in the Southern Hemisphere. It is approximately flat north of the equator but is red south of the equator, except at low frequency where it flattens at all latitudes, at a level that quadratically decreases from the northern to the southern boundary.

In the Southern Hemisphere, the spectral troughs and peaks at intermediate frequencies (Fig. 3, bottom) are related to the local Rossby waves, as the meridional transport due to the waves approximately vanishes when the frequency of the forcing equals a multiple of the ratio of the wave speed to the width of the basin, so that one or several wavelengths fit in the basin. Conversely the interior transport is maximum when the basin width equals 1/2, 3/2, . . . wavelengths. Note that the troughs and peaks are shifted to slightly longer periods than estimated from the Rossby wave transit time, as the waves are forced by the red spectrum in Fig. 2, and that the sharp peak at 1.5-month period is due to the equatorial mode.

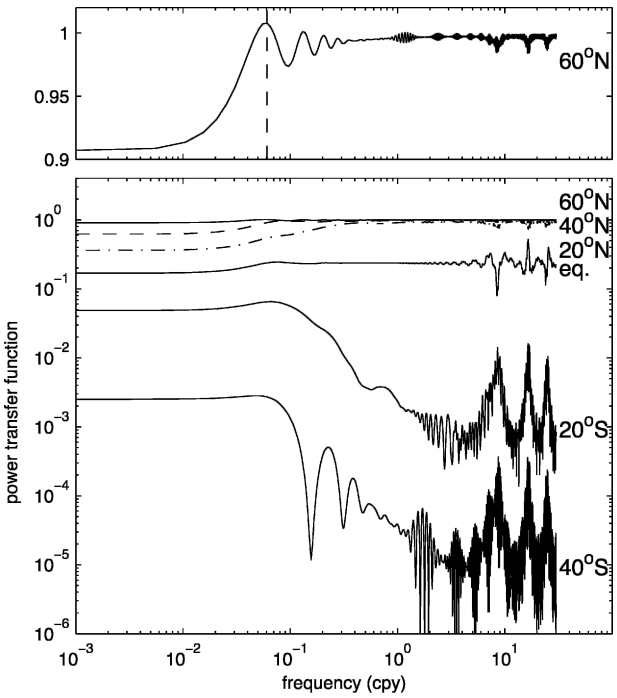

FIG. 3. Power transfer function for the meridional transport: $D_T(y,\omega)=S_T(y,\omega)/S_{TN}(\omega)$, at (top) 60°N with linear axis, and (bottom) at several latitudes with logarithmic axis (the transports at 40° and 20°N are represented with dashed and mixed lines, respectively). The dashed vertical line (top) indicates the period of the gravest eigenmode.

A close up of the transport power transfer function at 60°N (Fig. 3, top) reveals a peak at the period of the gravest eigenmode of the basin, consistent with Johnson and Marshall (2004, their Fig. A1). However, the basin mode only has little energy (note the linear scale) and it cannot be detected at low latitude. Hence, it is not significantly excited by changes in deep-water formation.

To explain the meridional transport spectra, we must separate the contribution of the western boundary current from that of the interior. Coastal Kelvin waves propagate (infinitely fast in our model) along the western boundary from the northern boundary to the equator, then along the equator until the eastern boundary, and poleward along the eastern boundary while exciting long Rossby waves. Along the southern boundary, the Kelvin waves propagate westward, and then northward along the western boundary, until they reach the equator. Because of the boundary conditions, the associated meridional transport in the western boundary layer is thus much larger in the Northern Hemisphere than in the Southern Hemisphere and it has the opposite sign across the equator. At high frequency, the transport mostly takes place in the western boundary layer of the Northern Hemisphere, and the equator acts as an efficient buffer. As the frequency decreases, the interior contributes increasingly to the transport, with a sign opposite to that in the western boundary layer. This slightly decreases the total transport in the Northern Hemisphere, but increases that in the Southern Hemisphere as the western boundary layer transport becomes smaller than the interior one. When the

Rossby waves reach the western boundary, they alter the western boundary layer transport, the interior becomes adjusted, and the interior transport decreases. The adjustment proceeds farther away from the equator as the frequency decreases, while the associated western boundary layer transport increases as more Rossby waves reach the western boundary. In the Northern Hemisphere, this decreases the transport in the western boundary layer so that the total transport keeps decreasing. In the Southern Hemisphere, the western boundary layer transport first decreases, then changes sign at a latitude that migrates southward as the frequency decreases, and increases in the opposite direction north of this latitude. Thus, at a fixed latitude, the total transport keeps increasing with decreasing frequency. At periods much longer than the Rossby waves transit time across the basin, the basin interior is adjusted and the conservation of mass (5) becomes

$$\left[\frac{\partial h_e}{\partial t}(t) + \lambda h_e(t)\right] \times \int_0^{L_x} \exp\left\{-\lambda\left[\frac{L_x - x}{c(y)}\right]\right\} dx = -\frac{\partial}{\partial y} T(y, t). \quad (18)$$

Since, for our basin, one has $\lambda L_x/c(y) \leq 0.19$,

$$\int_0^{L_x} \exp\left\{-\lambda\left[\frac{L_x - x}{c(y)}\right]\right\} dx = \frac{c(y)}{\lambda} \times \left\{1 - \exp\left[-\lambda \frac{L_x}{c(y)}\right]\right\}$$

approximately reduces to L_x. Thus, at low frequency, a quasi–steady state is established in which the transport varies linearly with latitude, and the equator no longer plays a role.

The relative contribution of the transport in the interior T_I and in the western boundary layer T_{BL} can be found away from the equator by comparing the spectrum of the total transport T with that of T_I (Fig. 4). At all frequencies, this ratio, noted R_I, is larger than 1 in the Northern Hemisphere but smaller than 1 in the southern part of the basin, tending to 0 as y tends to y_s [as $T(y_s) = 0$]. The latitude at which $R_I = 1$ migrates southward when frequency decreases as more Rossby waves reach the western boundary, changing the sign of T_{BL}. The peaks indicate latitudes at which T_I approximately vanishes because an integer number of wavelengths fits in the interior.

In summary, because the transport in the Northern Hemisphere is dominated by that in the western boundary layer, which is closely related to the forcing, D_T depends little on frequency, although a small southward decrease is seen at periods larger than the Rossby wave transit time. At the equator, D_T is white at frequencies lower than that of the equatorial mode, because the Rossby wave transit time is very short and the transport is adjusted. In the Southern Hemisphere, D_T is red because the transport changes are controlled by the interior dynamics. However, at all latitudes, D_T flattens at low frequency at a level determined by the conservation of mass. Therefore the equator acts as a low-pass filter for the Southern Hemisphere, rather than as a simple buffer.

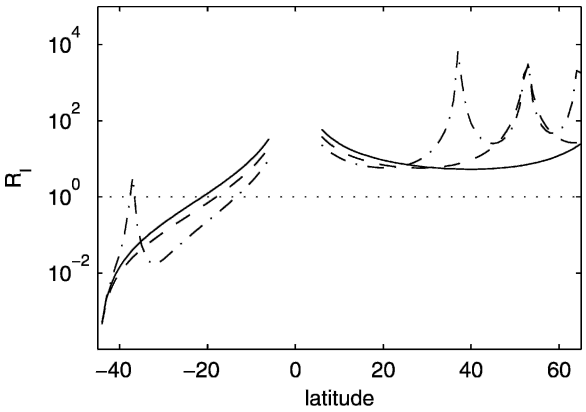

FIG. 4. Ratio of the spectrum of the total transport over that of the interior transport: $R_I(y, \omega) = S_T(y, \omega)/S_{T_I}(y, \omega)$ as a function of latitude at a period of 20 yr (plain line), 10 yr (dashed line), and 5 yr (mixed line).

4. Global variability

As a simplification of the global oceans, we consider the case of two basins connected by a periodic channel at their southern edge (Fig. 5). For basin A, the model is the same as before, except that the southern boundary is open. Basin P has a closed northern boundary and

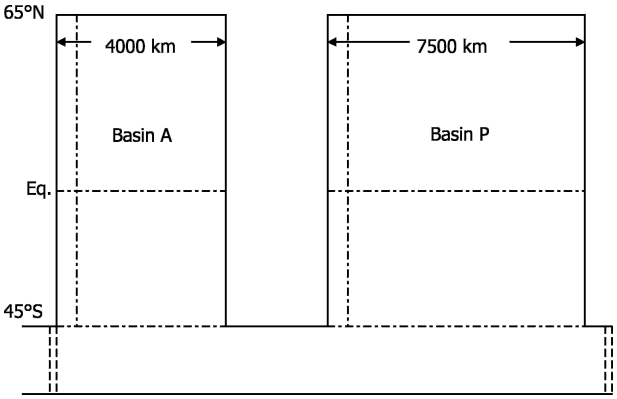

FIG. 5. Geometry for the two-basin case. The circumpolar channel is periodic, between the double dashed lines.

an open southern boundary. Using (10), the meridional transport at the southern boundaries are

$$TS_A(t) = \frac{g'H}{f(y_s)}[h_{eA}(t) - h_A(0, y, t)] \quad \text{and}$$

$$TS_P(t) = \frac{g'H}{f(y_s)}[h_{eP}(t) - h_P(x_w, y, t)], \tag{19}$$

where the subscripts indicate the basin and x_w is the western boundary of basin P.

In the southern channel, the perturbations are transmitted from basin to basin by coastal Kelvin waves that propagate eastward along the southern tip of the continents. Kelvin waves are not represented in the model, but they are implicitly taken into account by an instantaneous adjustment. Assuming that there is no mass source in the channel (or equivalently that the channel is infinitely thin) one has $h_A(0, y, t) = h_{eP}(t)$ and $h_p(x_w, y, t) = h_{eA}(t)$, which implies $TS_A(t) = -TS_P(t)$. A local source of deep water could be added in the southern channel to represent deep-water formation in the southern ocean. However, Nof (2003) has shown that the wind stress in the channel must be taken into account in order to evaluate the impact of a southern source of deep water on the transport at the southern limit of the two basins, which goes beyond the scope of this paper.

Mass conservation in each basin is obtained by integrating (6) and using (19), yielding

$$h_{eA}(t) = \frac{1}{\int_{y_s}^{y_n} c(y)\,dy} \times \left\{ \int_{y_s}^{y_n} c(y) h_{eA}\left[t - \frac{L_A}{c(y)} \right] \exp\left[-\lambda \frac{L_A}{c(y)} \right] dy - T_N(t) + \frac{g'H}{f(y_s)}[h_{eA}(t) - h_{eP}(t)] \right\} \quad \text{and} \tag{20}$$

$$h_{eP}(t) = \frac{1}{\int_{y_s}^{y_n} c(y)\,dy} \times \left\{ \int_{y_s}^{y_n} c(y) h_{eP}\left[t - \frac{L_P}{c(y)} \right] \exp\left[-\lambda \frac{L_P}{c(y)} \right] dy + \frac{g'H}{f(y_s)}[h_{eP}(t) - h_{eA}(t)] \right\}. \tag{21}$$

After Fourier transform, these equations can be combined to obtain the power transfer function $D_{h_{eA}}(\omega)$ and $D_{h_{eP}}(\omega)$ (thin lines in Fig. 2); $D_{h_{eA}}(\omega)$ is the same as in the one-basin case at high frequency, but the energy level is lower at low frequencies because of the energy leakage into basin P (the smaller basin P is, the smaller the decrease is). The spectral flattening still occurs at millennial periods as it is set by vertical diffusivity. In basin P, the spectral decay at intermediate frequencies is steeper because basin P is similar to a one-basin case forced (at the southern boundary) by a transport with a red spectrum. At low frequencies, $D_{h_{eP}}$ is slightly weaker than $D_{h_{eA}}$ because of the added dissipation of the signal coming from basin A, which occurs along the westward pathway of the Rossby waves in basin P (the wider basin P is, the bigger the decrease is). At high frequency, the power transfer function is much lower in basin P, consistent with Johnson and Marshall (2004, their Fig. 3). As in basin A, there are peaks, but they reflect the combined effects of the equatorial modes of the two basins.

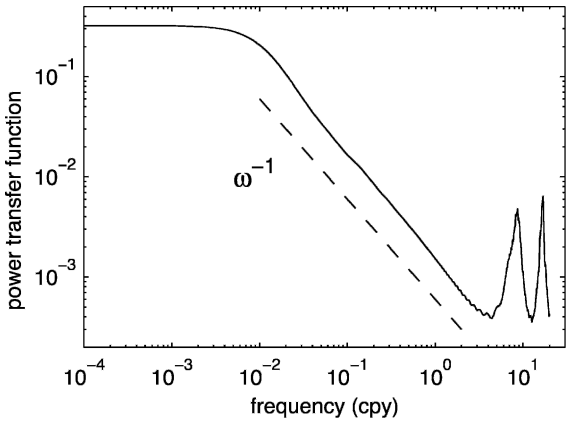

FIG. 6. Power transfer function for the transport between the two basins: $D_{TS}(\omega) = S_{TS}(\omega)/S_{TN}(\omega)$. The dashed line indicates an ω^{-1} law.

The power transfer function for the mass transport between the two basins, $D_{TS}(\omega)$, is derived from (19) and represented in Fig. 6. The peaks at high frequency mostly reflect the equatorial modes of basin A, as those of basin P are much less energetic. For periods from approximately 1 to 80 yr, D_{TS} approximately behaves as ω^{-1} and there is no prevailing time scale. The flattening at frequencies $\lesssim 10^{-2}$ cpy reveals that the adjustment between the two basins takes approximately 100 years, which is consistent with Huang et al. (2000). As h_{eP}, which is induced by h_{eA}, influences the latter in return [see (20)], it takes more than the Rossby waves transit time across the basins for the transport to be adjusted. However the effect is weak and the effective adjustment time of the two basins is about 2 times as long as the combined Rossby waves' transit time.

Note that the power transfer function for the transport in basin A in the two-basin case differs from that in the one-basin case for the level of stabilization at low

frequency. However, the general shape of the spectra is similar (not shown).

5. One-basin response to a more realistic forcing

The variability in deep-water formation has been represented by changes in the meridional transport at the northern boundary. If this transport were behaving as a white noise, then the preceding results for the power transfer functions would directly apply to the response spectra. However, deep-water formation and the induced meridional transport do not have white spectra, but reflect the integration of the atmospheric forcing by the upper ocean, the influence of preconditioning, and that of the subpolar North Atlantic circulation; thus they involve complex dynamics and various feedback processes.

As a first step toward using a more realistic forcing spectrum, monthly time series of the mixed layer volume in a deep convection region were derived from two simulations with an oceanic general circulation model (OGCM), the global Nansen Center version (Bentsen et al. 2004) of Miami Isopycnic Coordinate Ocean Model (MICOM; Bleck et al. 1992), and then used to coarsely represent the variability of deep-water formation.

The first simulation is at rather high resolution (but not eddy resolving). It is based on a regional version of MICOM with 20-km horizontal resolution covering the Atlantic Ocean between 30° and 78°N, nested in a global version of double horizontal resolution and forced by daily fields derived from the National Centers for Environmental Prediction–National Center for Atmospheric Research (NCEP–NCAR) reanalyses from 1948 to 2002. The global simulation is discussed in Bentsen et al. (2004); the nesting approach and the regional simulation are discussed in Hátun et al. (2005). Although deep convection occurs in the Labrador Sea, the Irminger Sea, and the Greenland, Iceland, and Norwegian (GIN) Seas, we only consider convection in the Labrador Sea. The latter is assumed to occur where the standard deviation of the mixed layer depth exceeds 520 m in March, which approximately corresponds to the convection region seen in the observations (Marshall and Schott 1999). The winter deepening of the mixed layer in this region, which leads to deep-water formation, clearly appears in the top of Fig. 7. The monthly anomalies from the mean annual cycle of the mixed layer volume were taken to represent the anomalies of the produced deep water, an admittedly crude assumption. The standard deviation of the time series is 2.6 Sv (Sv $\equiv 10^6$ m^3 s^{-1}), consistent with observational estimates of Rhein et al. (2002), who found

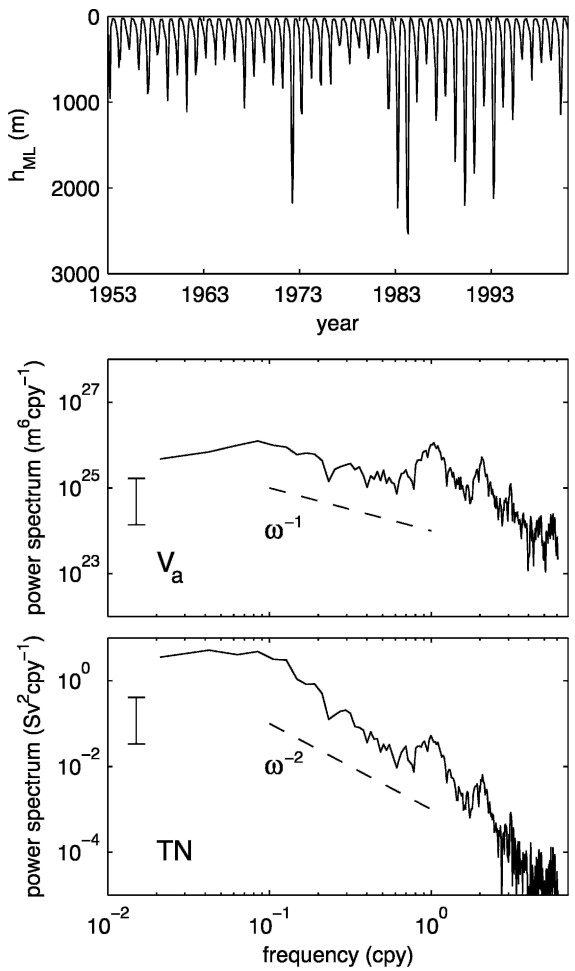

FIG. 7. Time series of the (top) mean mixed layer depth in the Labrador Sea region of convection in the forced simulation (h_{ML}), (middle) power spectrum of the corresponding volume anomalies of mixed layer water (V_a), and (bottom) induced meridional transport (T_N). The spectra are calculated with the multitaper method using three windows, and the 95% confidence interval is given. Dashed lines indicate power laws.

fluctuations of the Labrador Sea Water formation rate of about 3 Sv. The power spectrum (Fig. 7, middle) has broad peaks at the annual period and its multiple is induced by the annual modulation of the mixed layer variability and it is slightly red down to the decadal period where it flattens or slightly decreases. However, the run is too short to characterize the low-frequency behavior, which will be done below by using the coarser version of the model.

The link between deep-water formation and southward deep transport has not been clearly established. However, Straneo et al. (2003) developed an advective–diffusive model of the spreading of Labrador Sea Water based on Lagrangian data, which gives spreading time scales of Labrador Sea Water in reasonable agreement

with the observations. As this model is linear, it gives a linear relationship between the volume of convected water in the Labrador Sea and the induced transport in the deep western boundary current (their Fig. 11): the transport is negligible until approximately six months after a flush of deep water, when it suddenly reaches its maximum, and then exponentially decays with an *e*-folding time of 6 yr. This can be modeled by a linear transfer function, the maximum of the transport being determined by the conservation of the volume. As we are interested in the variability of the deep western boundary current, we apply the model to the volume anomalies above of convected water, which are regarded as a succession of (positive or negative) flushes of deep water. The deep southward transport anomaly at any given time step is thus given by the contributions from all of the prior deep-water flushes. The fluctuations are on the order of 2 Sv and their power spectrum is red, approximately behaving as ω^{-2} for periods from 4 months to 5 years (Fig. 7, bottom). As the linear transfer function integrates the input, it favors low-frequency variability. The flattening at low frequency suggests that the derived deep western boundary current has maximum variance at decadal periods. The peaks at the annual period and its multiple again reflect the cyclostationarity of convection.

To better resolve the low frequencies, we also considered a control integration of the Bergen Climate Model (Furevik et al. 2003): the middle 200 years of the simulation considered by Mignot and Frankignoul (2005). The ocean component is the same as before, but with a much coarser resolution (40 km). Again, we consider the monthly anomalies of the mixed layer volume in the region of Labrador Sea convection. The standard deviation of the derived southward transport anomalies is about 10 Sv, which is much larger than the estimates above, largely because the region where convection may take place is much broader at coarse resolution. As a result, the power spectrum of the inferred transport is of unrealistic amplitude, but it has the same shape as that from the forced simulation in the frequency range resolved by the latter (Fig. 8, top). However, the spectrum does not flatten, as in Fig. 7 (bottom), except slightly at much lower frequency (but note that the time series had been detrended by a third-order polynomial).

To force our linear model, we use the 200-yr T_N time series. As a higher sampling was needed to represent the equatorial mode, it was interpolated using a cubic spline, which explains the fast high-frequency decay in Fig. 8 (top). The spectrum of h_e is shown for the one-basin case in Fig. 8 (bottom). Since the model is linear, it is obtained by multiplying the forcing spectrum with

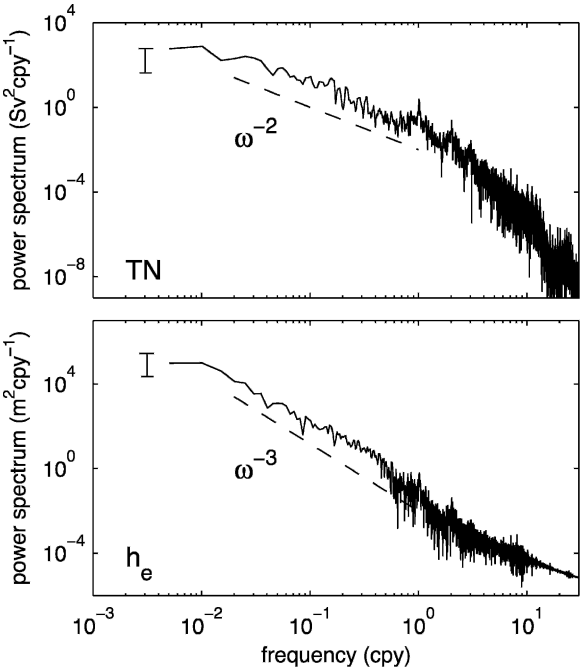

FIG. 8. Power spectrum of (top) T_N extracted from the coupled simulation and (bottom) h_e, calculated with the multitaper method using three windows. The 95% confidence interval is given. Dashed lines indicate power laws.

the power transfer function in Fig. 2. Between periods from 1 to 50 yr, the spectrum of h_e broadly behaves as ω^{-3}, which simply results from the approximate ω^{-1} slope of the power transfer function multiplied by the ω^{-2} slope of the forcing. The strength of the equatorial mode is considerably attenuated because the forcing is weak at high frequencies. Overall, most of the variance of h_e is found at low frequencies. Because of the flattening in the transfer function at periods larger than 1000 years, the spectrum of h_e should become white at very low frequencies, and the prevailing time scales thus range between 10 and 1000 yr.

The spectrum of the meridional transport is represented at 40°N and 30°S in Fig. 9. As expected, the spectrum of the transport at 40°N is very similar to that of the forcing, with a red behavior and small peaks at the annual period and its multiples. At 30°S, the energy level is lower than at 40°N by about two orders of magnitude at low frequency and by up to four orders of magnitude at high frequency. This results in a redder spectrum at 30°S than at 40°N, consistent with Fig. 3.

In both hemispheres, the predicted transport spectrum is slightly red for periods longer than a few years. This is consistent with the variability of deep ocean mass transport in several coupled ocean–atmosphere models, as discussed in von Storch et al. (2000), where the spectra of the zonally averaged streamfunction at

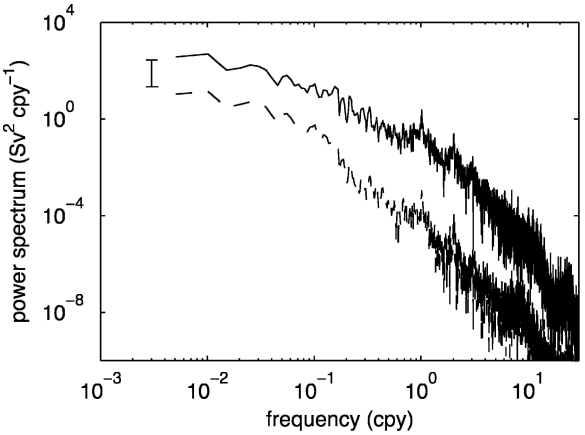

FIG. 9. As in Fig. 8 but for the power spectrum of the meridional transport at 40°N (plain line) and 30°S (dashed line).

depth have a spectral slope of −1 to −2 at low frequency. Our prediction is also in broad agreement with the Bergen Climate Model where the MOC has an approximate ω^{-1} behavior at low frequency (Bentsen et al. 2004). However, as shown in Fig. 10, there is more variance at interdecadal periods in the North Atlantic, and the MOC spectrum becomes approximately white at high frequencies, presumably because of the influence of wind forcing that was neglected in our study. Figure 10 also shows that in the Bergen Climate Model the variability of the MOC is weaker in the Southern Hemisphere than in the Northern Hemisphere, in qualitative agreement with our prediction, although the power density decrease is smaller in the coupled model, possibly because of the influence of other sources of deep water.

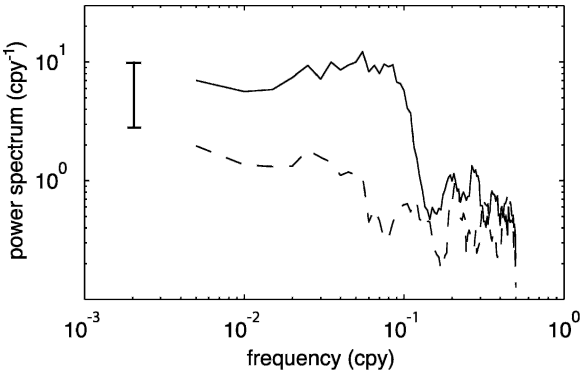

FIG. 10. Power spectrum of the maximum of the streamfunction at 40°N (plain line) and 30°S (dashed line), from 200 years of a control simulation with the Bergen Climate Model (from Mignot 2003). The time series were detrended by a cubic polynomial. The 90% confidence interval is indicated.

6. Conclusions

A linear reduced-gravity model was used in idealized basins to explore the role of ocean dynamics in setting the spectral characteristics of the response of the MOC to the variability of deep-water formation. The latter was represented by stochastic changes in the meridional transport at the northern boundary of the domain. The Kelvin waves, which propagate the perturbations along the boundaries, were assumed to be infinitely fast. In the one-basin case, the power transfer function (or equivalently, the response power spectrum if the forcing is white) for the thermocline depth perturbations in the interior was shown to be red, with a flattening at periods larger than 1000 yr as a result of damping by the vertical diffusivity. In addition, there are sharp spectral peaks at high frequencies due to an equatorial mode, which was observed in a more complex model by Cane and Moore (1981), who stressed, however, that more realistic conditions, including the mean equatorial currents, are a serious impediment to its existence in the world's oceans.

The meridional transport in the Northern Hemisphere is directly influenced by the forcing via the western boundary current, and its power transfer function is approximately white. In the Southern Hemisphere, the interior dynamics dominate, which favors low frequencies. This asymmetry is due to the influence of the equator. At high frequency, the transport mostly takes place in the western boundary layer of the Northern Hemisphere, and the equator acts as an efficient buffer. As the Rossby waves propagate westward, the interior transport increases, and so does the total transport in the Southern Hemisphere, while the transport slightly decreases in the Northern Hemisphere. As the frequency decreases, the interior approaches adjustment and the interior transport decreases. However, the transport induced by the Rossby waves in the western boundary layer increases, slightly reducing the transport in the western boundary layer of the Northern Hemisphere, but dominating that in the Southern Hemisphere. As a result, the total transport decreases with decreasing frequency in the Northern Hemisphere, and increases in the Southern Hemisphere, until a quasi–steady state is reached in which the transport vary approximately linearly with latitude. The equator no longer plays a role, and therefore acts as a low-pass filter, which clarifies the equatorial buffering effect discussed in JM02.

Because of the strong damping caused by the latitudinal variation in the Rossby waves transit time, the low-frequency basin modes are not significantly excited by changes in deep-water formation: the modes have a

very small amplitude, but they were detected at very high latitude in the Northern Hemisphere. Note that Lacasce and Pedlosky (2004) showed that the instability of the long Rossby waves would prevent resonance at high latitudes, so the mode may not be seen at all in a more realistic model.

The extension of the model to the two-basin case shows that another basin connected via a southern channel has little influence on the response in the basin directly forced by deep-water formation, which is very similar to that in the one-basin case. The spectra are redder in the second basin because it is forced by the meridional transport at the southern limit of the first basin, which has a red spectrum. Because of the weak influence of the second basin on the forced basin, the adjustment time is approximately 2 times the Rossby waves' transit time across the two basins. Thus the two basins are adjusted at periods longer than 100 yr, consistent with Huang et al. (2000).

To obtain a somewhat realistic forcing spectrum, time series of the anomalies of the mixed layer volume in the region of deep-water formation in the Labrador Sea were constructed from two simulations with the Nansen Center version of MICOM, a high-resolution version forced by daily NCEP–NCAR reanalyses and a lower-resolution one used in a control run with the Bergen Climate Model. The volume anomalies were assumed to represent the changes in deep-water formation and they were related to the induced meridional transport using a simple model derived from Straneo et al. (2003). Since the data are based on rather realistic simulations, the derived transport implicitly includes the effect of the atmospheric forcing, the preconditioning, advection, and the various feedback processes that affect deep-water formation. Its power spectrum is red and similar in the two cases. Using the derived transport to force our model gives even redder response spectra so that the equatorial mode is strongly attenuated. At low frequency, the spectrum of the meridional transport has a spectral slope between -1 and -2 but no spectral peaks, and the power density is much smaller in the Southern Hemisphere than in the Northern Hemisphere. These features are in qualitative agreement with the low-frequency variability of the MOC in various coupled models. A more quantitative comparison was not attempted, since no other source of deep-water formation was considered, although the variability of the overflow from the GIN Seas might introduce a specific time scale in the MOC (Döscher et al. 1994), nor was the wind forcing taken into account, which may contribute to the decadal variability of the MOC.

Acknowledgments. We thank Jerome Sirven for stimulating discussions, Helge Drange and Juliette Mignot for providing the OGCM data, and the two anonymous reviewers for helpful comments. We acknowledge support (to CF) from the Institut Universitaire de France.

REFERENCES

Bentsen, M., H. Drange, T. Furevik, and T. Zhou, 2004: Simulated variability of the Atlantic meridional overturning circulation. *Climate Dyn.,* **22,** 701–720.

Bleck, R., C. Rooth, D. Hu, and L. T. Smith, 1992: Salinity-driven thermocline transients in a wind- and thermohaline-forced isopycnic coordinate model of the North Atlantic. *J. Phys. Oceanogr.,* **22,** 1486–1505.

Boyle, E. A., 2000: Is ocean thermohaline circulation linked to abrupt stadial/interstadial transitions? *Quat. Sci. Rev.,* **19,** 255–272.

Cane, M. A., and D. W. Moore, 1981: A note on low frequency equatorial basin modes. *J. Phys. Oceanogr.,* **11,** 1578–1584.

Cessi, P., and S. Louazel, 2001: Decadal oceanic response to stochastic wind forcing. *J. Phys. Oceanogr.,* **31,** 3020–3029.

——, and F. Primeau, 2001: Dissipative selection of low-frequency modes in a reduced-gravity basin. *J. Phys. Oceanogr.,* **31,** 127–137.

——, and P. Otheguy, 2003: Oceanic teleconnections: Remote response to decadal wind forcing. *J. Phys. Oceanogr.,* **33,** 1604–1617.

Delworth, T., and R. J. Greatbatch, 2000: Multidecadal thermohaline circulation variability driven by atmospheric surface flux forcing. *J. Climate,* **13,** 1481–1495.

——, S. Manabe, and R. J. Stouffer, 1993: Interdecadal variations of the thermohaline circulation in a coupled ocean–atmosphere model. *J. Climate,* **6,** 1993–2011.

Döscher, R., C. W. Böning, and P. Herrmann, 1994: Response circulation and heat transport in the North Atlantic to changes in thermohaline forcing in northern latitudes: A model study. *J. Phys. Oceanogr.,* **24,** 2306–2320.

Eden, C., and J. Willebrand, 2001: Mechanism of interannual to decadal variability of the North Atlantic circulation. *J. Climate,* **14,** 2266–2280.

Furevik, T., M. Bentsen, and H. Drange, 2003: Description and evaluation of the Bergen climate model: ARPEGE coupled with MICOM. *Climate Dyn.,* **21,** 27–51.

Ganachaud, A., and C. Wunsch, 2000: Improved estimates of global ocean circulation, heat transport and mixing from hydrographic data. *Nature,* **408,** 453–457.

Hátun H., A. B. Sando, H. Drange, and M. Bentsen, 2005: Seasonal to decadal temperature variations in the Faroe-Shetland inflow waters. *The Nordic Seas: An Integrated Perspective, Geophys. Monogr.,* No. 158, Amer. Geophys. Union, 370 pp.

Huang, R. X., M. A. Cane, N. Naik, and P. Goodman, 2000: Global adjustment of the thermocline in response to deepwater formation. *Geophys. Res. Lett.,* **27,** 759–762.

Johnson, H. L., and D. P. Marshall, 2002a: A theory for the surface Atlantic response to thermohaline variability. *J. Phys. Oceanogr.,* **32,** 1121–1132.

——, and ——, 2002b: Localization of abrupt change in the North Atlantic thermohaline circulation. *Geophys. Res. Lett.,* **29,** 1083, doi: 10.1029/2001GL014140.

——, and ——, 2004: Global teleconnections of meridional overturning circulation anomalies. *J. Phys. Oceanogr.,* **34,** 1702–1722.

Kawase, M., 1987: Establishment of deep ocean circulation driven by deep-water production. *J. Phys. Oceanogr.,* **17,** 2294–2317.

Lacasce, J. H., 2000: Baroclinic Rossby waves in a square basin. *J. Phys. Oceanogr.,* **30,** 3161–3178.

——, and J. Pedlosky, 2004: The instability of Rossby basin modes and the oceanic eddy field. *J. Phys. Oceanogr.,* **34,** 2027–2041.

Latif, M., E. Roeckner, U. Mikolajewicz, and R. Voss, 2000: Tropical stabilization of the thermohaline circulation in a greenhouse warming simulation. *J. Climate,* **13,** 1809–1813.

Manabe, S., and R. J. Stouffer, 1999: The role of thermohaline circulation in climate. *Tellus,* **51,** 91–109.

Marshall, J. C., and F. Schott, 1999: Open-ocean convection: Observations, theory and models. *Rev. Geophys.,* **37,** 1–64.

Mauritzen, C., and S. Häkkinen, 1999: On the relationship between dense water formation and the "Meridional Overturning Cell" in the North Atlantic Ocean. *Deep-Sea Res. I.,* **46,** 877–894.

Mignot, J., 2003: Sur la variabilité climatique de la salinité de surface en Atlantique Nord et son lien avec la circulation océanique dans un modèle couplé. Ph.D. thesis, Université Paris VI, 194 pp.

——, and C. Frankignoul, 2005: The variability of the Atlantic meridional overturning circulation, the North Atlantic Oscillation, and the El Niño–Southern Oscillation in the Bergen Climate Model. *J. Climate,* **18**, 2361–2375.

Nof, D., 2003: The Southern Ocean's grip on the northward meridional flow. *Progress In Oceanography,* Vol. 56, Elsevier Press, 223–247.

Percival, D. B., and A. T. Walden, 1993: *Spectral Analysis for Physical Applications: Multitaper and Conventional Univariate Techniques.* Cambridge University Press, 583 pp.

Primeau, F., 2002: Long Rossby wave basin-crossing time and the resonance of low-frequency basin modes. *J. Phys. Oceanogr.,* **32,** 2652–2665.

Rahmstorf, S., 1997: Influence of Southern Hemisphere winds on NADW flow. *J. Phys. Oceanogr.,* **27,** 2040–2054.

Rhein, M., and Coauthors, 2002: Labrador Sea Water: Pathways, CFC inventory, and formation rates. *J. Phys. Oceanogr.,* **32,** 648–665.

Schott, F., R. Zantopp, L. Stramma, M. Dengler, J. Fischer, and M. Wibaux, 2004: Circulation and deep water export at the western exit of the subpolar North Atlantic. *J. Phys. Oceanogr.,* **34,** 817–843.

Stommel, H., and A. B. Arons, 1960: On the abyssal circulation of the World Ocean. I. Stationary planetary flow patterns on a sphere. *Deep-Sea Res.,* **6,** 140–154.

Straneo, F., R. S. Pickart, and K. Lavender, 2003: Spreading of Labrador Sea Water: An advective-diffusive study based on Lagrangian data. *Deep-Sea Res. I.,* **50,** 701–719.

Timmermann, A., and M. Latif, 1998: Northern Hemispheric interdecadal variability: A coupled air–sea mode. *J. Climate,* **11,** 1906–1931.

Vellinga, M., and P. Wu, 2004: Low-latitude freshwater influence on centennial variability of the Atlantic thermohaline circulation. *J. Climate,* **17,** 4498–4511.

von Storch, J.-S., P. Müller, R. J. Stouffer, R. Voss, and S. F. B. Tett, 2000: Variability of deep-ocean mass transport: Spectral shapes and spatial scales. *J. Climate,* **13,** 1916–1935.